Materials & Design 213 (2022) 110328

Contents lists available at ScienceDirect

Materials & Design

journal homepage: www.elsevier.com/locate/matdes

A differential evaporation model to predict chemistry change of additively manufactured metals

Meelad Ranaiefar [a,*], Pejman Honarmandi [a], Lei Xue [a], Chen Zhang [b], Alaa Elwany [b], Ibrahim Karaman [a], Edwin J. Schwalbach [c], Raymundo Arroyave [a]

[a] Texas A&M University, Department of Materials Science and Engineering, College Station, TX 77840, USA
[b] Texas A&M University, Wm Michael Barnes'64 Department of Industrial and Systems Engineering, College Station, TX 77840, USA
[c] Air Force Research Laboratory, Materials and Manufacturing Directorate, Wright-Patterson Air Force Base, OH 45433, USA

HIGHLIGHTS

- An integrated computational framework is developed to predict material properties.
- Thermal model parameter values and uncertainties are evaluated with an MCMC method.
- Chemistry and property predictions are in good agreement with experiment results.

GRAPHICAL ABSTRACT

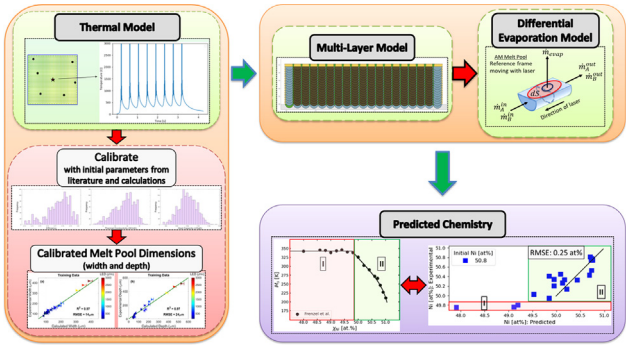

ARTICLE INFO

Article history:
Received 6 October 2021
Revised 5 December 2021
Accepted 16 December 2021
Available online 18 December 2021

Keywords:
Additive manufacturing
Markov chain Monte Carlo
Differential evaporation
NiTi
Shape memory alloys
Bayesian calibration
4D printing

ABSTRACT

The desire for increased performance and functionality has introduced additional complexities to the design and fabrication of additively manufactured (AM) parts. However, addressing these needs would require improved control over local properties using in-line feedback from fast-acting low-fidelity models during the fabrication process. In this regard, differential evaporation is an inherent characteristic in metal AM processes, directly influencing local chemistry, material properties, functionality, and performance. In the present work, a differential evaporation model (DEM) is presented for laser powder bed fusion (LPBF) AM to predict and control the effect of evaporation on chemistry and properties on local and part-wide scales. The DEM model is coupled with an analytical thermal model that is calibrated against 51.2 Ni [at%] nickel titanium shape memory alloy (NiTi SMA) single-track experiments and a multi-layer model that accounts for the AM part's multi-layer design and the inherent melt pool overlap and chemistry propagation. The combined hierarchical model, consisting of the thermal, evaporation, and multi-layer components, is used to predict location-specific chemistry for LBPF AM fabrication of $Ni_{50.8}Ti_{49.2}$ [at%] SMAs. Model predictions are validated with values obtained from multi-layer experiments on a commercial LPBF system, resulting in a root mean square error (RMSE) of 0.25 Ni [at%] for predicted Ni content. Additionally, martensitic transformation temperature, M_s, is calculated and compared with empirical data, resulting in an RMSE of 18.6 K. A practical account of the cumulative and propagative thermal-induced evaporation effect on location-specific chemistry is made through this linkage of models. Fundamentally, this model chain has also provided a solution to the forward modeling problem,

* Corresponding author at: Texas A&M University, Department of Materials Science and Engineering, 3003 TAMU, College Station, TX 77843-3003, USA.
E-mail address: mranaiefar@tamu.edu (M. Ranaiefar).

https://doi.org/10.1016/j.matdes.2021.110328

enabling steps to be taken towards resolving the inverse design problem of determining processing parameters based on desired location-specific properties.

1. Introduction

Additive manufacturing (AM) of functional and structural materials has received increased attention to meet the demand for specialty components in the aerospace, automotive, and medical industries [1–4]. Through design optimization and improved control over the AM process, components with improved performance and functional properties have been successfully fabricated from materials such as Ti-6Al-4V, stainless steels, and NiTi shape memory alloys (SMAs), among many others. AM has been traditionally regarded as a manufacturing method that can be used to fabricate components with high degrees of geometric complexity. While this is certainly true, much larger (and rather underutilized) potential lies in achieving material complexity through effectively modulating and controlling underlying mechanisms associated with the complex AM process. One such mechanism that can be harnessed to achieve location-specific control of properties and improved component quality of AM tailor-designed parts is differential evaporation.

Several studies involving laser processing of Ti-6Al-4V and stainless steels have shown that differential evaporation influences the post-process composition of a part [5–7], leading to a change in functional and structural properties. In the case of NiTi, Khan et al. demonstrated that laser processing of NiTi (50.07 at% Ni) SMA resulted in Ni depletion and an outcome of (48.36 ± 0.84) [at%] Ni [8]. The processed region also experienced a microstructural change from austenite to martensite, and Ti_2Ni precipitates were found in the processed region due to Ti's insolubility in the Ni depleted region. The significant influence of evaporation on functional properties is then exhibited through changes of 1 [at%] Ni resulting in (80–100) K changes in transformation temperature for Ni compositions above 50 at% [9,10]. Ma et al. [11,12] captured this process-structure-property relationship in NiTi by changing hatch spacing during laser-based AM from 35 μm to 120 μm for two sections of a monolithic NiTi part. This alteration and the change in the resulting volumetric energy density (VED) input translates to a distinct difference in thermal history, the magnitude of evaporation, and post-process chemistry. Indeed, this resulted in a difference of 60 K in transformation temperature for each section of the part, demonstrating the effect of evaporation on the chemistry and functional properties of an AM NiTi part [13].

Advancing the capability for tailored AM design would then require a comprehensive understanding of vaporization and the process-structure-property-performance (PSPP) relationship in AM. Fig. 1 illustrates the complexity of this PSPP relationship for SMA NiTi vaporization in AM. An AM part's final chemistry and properties are the culmination of a set of processing parameters and the repeated thermal processing of the initial powder composition, building track-after-track and layer-upon-layer. In principle, by controlling the process conditions at each location of the part, it would be possible to alter the local thermal history and affect the (differential) evaporation process. In the case of functional materials, such as NiTi-based SMAs, that are extremely sensitive to chemical and microstructural changes, such degree of local control could enable, for example, 4D printing of metallic components [11,14].

To explicitly leverage *differential evaporation* as a tool to provide location-dependent control over chemistry, microstructure, properties and behavior, it is necessary to develop formal design tools capable of transforming a desired (local) chemistry/microstructure into a required (local) processing protocol. The first necessary ingredient of such a design tool would be a suitable chain of *forward* models capable of connecting process conditions, thermal histories and chemistry changes due to differential evaporation. Experimental approaches to building such connections are impractical. High-fidelity numerical models are extremely costly, particularly when considering that simulations must be able to capture local changes in chemistry at the part level. One solution to this forward problem is the utilization of fast-acting, physically-rich (semi) analytical models calibrated and validated with experiments to provide relatively accurate simulations of the PSPP relationship for the sake of AM product design.

In order to quantify the effect of evaporation, the thermal history of an AM part must first be simulated through numerical or analytical solutions. These simulations can be performed to varying degrees of complexity and fidelity, with the tradeoff of computational cost. High-fidelity models have arisen from the need to address complex coupling present in the various mechanisms in place during AM. Such models may employ finite element [15–24], finite difference [25], or finite volume [26–28] methods. However, these high-fidelity solutions come at a high computational cost, limiting their utility for the AM design process [29,30] and parameter calibration [31]. For comprehensive exploration of the AM design space, a fast analytical model yielding an acceptable degree of fidelity and accuracy presents a desirable approach [32]. Linking this fast-acting thermal model with a cost-effective structural and property-based model in an integrated computational materials engineering (ICME) framework then enables the screening of trends in the (forward) PSPP of AM parts and can also aid the reverse PSPP linkage in product design.

In this study, a fast-acting thermal-history coupled differential-evaporation model is developed to predict the change in chemistry for laser powder bed fusion (LPBF) AM parts, as highlighted in green alongside corresponding depictions in Fig. 1. A follow-up study will then further explore and exploit this model to solve the inverse design problem, where inexpensive physically-rich models are applied to guide experiments. Model assumptions are presented, simulation and calibration of melt pool geometry discussed, a mass balance analysis is conducted, and considerations for evaporation rate are presented. In conjunction, an assessment of a multi-layer model accounting for geometric effects is provided. Model predictions for location-specific chemistry (Ni [at%]) are then validated with experiments and linked to material properties (martensite transformation temperature, M_s) - providing a complete path through the PSPP relationship and a solution to the forward design problem. NiTi SMA was chosen as the model material for this work due to its industrial relevance, functional properties, and vapor pressure difference among the alloying components ensuring a measurable change in post-process composition.

2. Thermal model calibration

2.1. Thermal model

The thermal model used in this study, a fast-acting analytical discrete source model (DSM), was developed and described in detail by Schwalbach et al. [33]. In the current work, directly relevant aspects of the DSM will be described briefly, but the reader is referred to the reference for more details. Additionally, this inex-

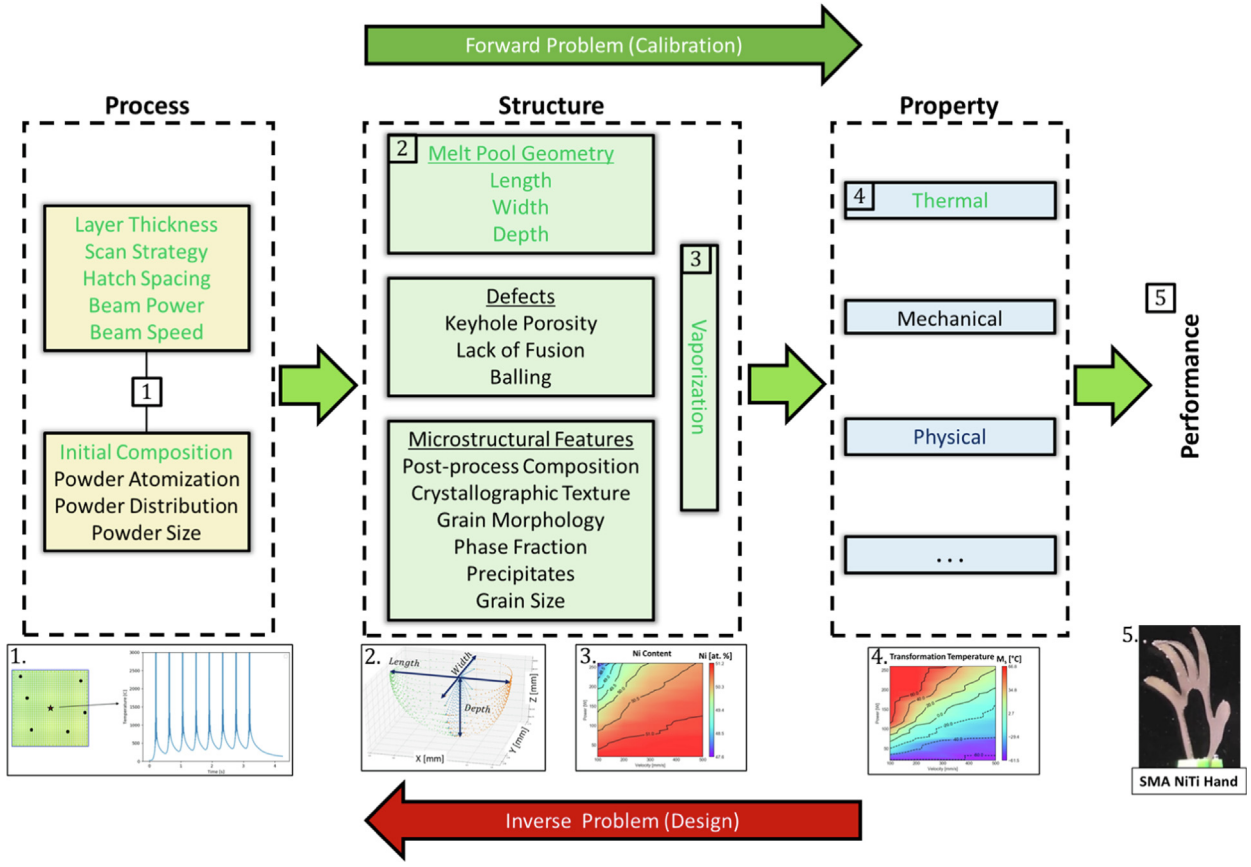

Fig. 1. Process-Structure-Property-Performance diagram toward the location control of properties and tailored design of AM fabricated parts. Components considered by the computational model in this work are highlighted in green. Modeling components include: Process to Structure - (1) Thermal Model; Structure to Property - (2) Multi-Layer Model, (3) Differential Evaporation Model, and (4) Ni-Transformation Temperature Relation. Property to Performance coupling can then be performed based on desired specifications and experiment results (5).

pensive low-fidelity model will be calibrated similar to [34], providing sufficiently accurate results for the purpose of this work. Although the individual models comprising the ICME framework in this study are generally modular, where a higher-fidelity model could instead be substituted in, this does not necessarily alleviate all calibration requirements, and computational cost must be balanced against fidelity requirements for the purposes of rapid design iterations.

2.1.1. Assumptions

This model's development begins with the generation of assumptions used to describe and simplify the physics involved in thermal history simulation and corresponding melt pool geometry during LPBF AM. These assumptions are broadly similar to those of the Rosenthal model of fusion welding, with the main exceptions that the heat source is allowed to move in an arbitrarily complex path, and that its shape is an elliptical 3D gaussian. The main model assumptions include:

1. Thermophysical properties are considered temperature independent, enabling model simplification. From a previous study by Schwalbach et al. [33], temperature dependency of material properties has a minimal effect on predicted melt pool characteristics. However, the distributions associated with their effective values are obtained after probabilistic model calibration against experiments to cover for any possible uncertainties resulting from this assumption.
2. Latent heat due to phase change is assumed to be less than the sensible heat during the thermal process. It is indirectly considered through a calibrated effective heat capacity parameter.
3. Heat transfer is directly governed by the heat conduction equation in the model, while the effects of radiation, evaporation, and convection to the gas are indirectly considered in the form of a tuning parameter called the efficiency parameter—which accounts for the material absorption efficiency as well. Moreover, the physically complex convection in the liquid and its effect on the melt pool shape is also indirectly implemented in the model through the consideration of a shape factor, i.e., the depth to width ratio of the volumetric heat source [35]. This ratio requires calibration for each individual experimental condition, but is assumed to be constant and equal to 1 in this work for simplicity. Accordingly, a physical depth correction factor is considered and calibrated against experiments for cases that the keyhole criterion is met—based on NiTi alloy printability maps [36]—in order to account for the significant effect of convection in these cases.
4. Scanning speed and power input are constant, as in the experimental setup, although the DSM is capable of handling arbitrary changes in these quantities if required.

Through these assumptions, a reduction in both fidelity and cost are incurred. This results in a model ideal for the purpose of screening for trends that will be used as a basis for experiments and materials design. However, in the interest of analyses requir-

ing extreme precision, the DSM may be exchanged with a thermal model of higher fidelity, but typically at increased cost.

2.1.2. Thermal history

In general, the DSM predicts the temperature at any specifically given position ($\vec{r}_j$) and process time (t) during the thermal process. It does this by considering the thermal energy input at the position from a series of volumetric discrete heat sources ($\vec{s} = \{s_1, \cdots, s_N\}$ that activate one by one during the process at $\vec{\tau} = \{\tau_1, \cdots, \tau_N\}$, respectively) and the energy conduction throughout the material, as follows:

$$\frac{\partial T}{\partial t} = D\nabla^2 T + \sum_{i=1}^{N} \frac{\hat{s}_i\left(\vec{r}_j, t\right)}{\rho C_p} \tag{1}$$

where T, ρ, and C_p are temperature, mass density, and mass specific heat capacity, respectively. D is thermal diffusivity, a temperature-independent parameter, and correlated to thermal conductivity (κ) as $D = \frac{\kappa}{\rho C_p}$.

Assuming the discrete heat sources have spherical normal-distribution shapes centered at $\vec{r}_i$s with standard deviations equal to σ, Eq. 1 becomes:

$$\frac{\partial T}{\partial t} = D\nabla^2 T + \sum_{i=1}^{N} \frac{2\eta_i P_i \Delta t}{\rho C_p (2\pi\sigma^2)^{1.5}} exp\left(-\frac{R_{ij}^2}{2\sigma^2}\right)\delta(t-\tau_i) \tag{2}$$

where η_i, known as efficiency, accounts for the material's energy absorptivity and, upon activation of the heat source i, energy losses due to radiation and evaporation. $\eta_i P_i$ is the effective power of heat source i, where P_i is the actual power of the heat source. It should be noted that η_i and P_i are assumed to be constant in this work, denoted as η and P. Δt is the source discretization time, $R_{ij} = |\vec{r}_j - \vec{r}_i|$ is the distance of the given position from source i, and δ is the Dirac delta function.

Solving Eq. 2 for an infinite uniform medium with initial temperature T_0 results in the temperature prediction at any given position and process time:

$$T\left(\vec{r}_j, t\right) = T_0 + \sum_{i=1}^{N}\left\{\frac{\eta_i P_i \Delta t}{\rho C_p \sqrt{2}\pi^{1.5}}\Theta(t-\tau_i)\left(\sigma^2 + 2D(t-\tau_i)\right)^{-1.5} \times \exp\left(-\frac{R_{ij}^2}{2(\sigma^2 + 2D(t-\tau_i))}\right)\right\} \tag{3}$$

where Θ is the Heaviside step function. For more details about the model formulation, see [33].

2.1.3. Melt pool geometry

The melt pool formed through the previously described interaction of the laser and material can define a controlled volume in the printing process, a vital step for evaluating the effect of evaporation. For the remainder of the work, it should be noted that the beam propagates along the Z-direction, and traverses the XY-plane of the powder bed along the X-direction. Assuming a quasi-steady state, the melt pool's extent at any location of interest is then determined based on solidification time. A radial vector search pattern centered about the location of interest provides a resolved 2D cross-section of the YZ-plane (width and depth) along with intermediary points, as shown in Fig. 2 (A). The solidification time for each coordinate, $t_{solid,yz}$, and laser velocity, u, may then be used to determine a length, L_B, representing the back portion of the melt pool:

$$L_{B,yz} = \left(t_{solid,yz} - t_{solid,min}\right)u \tag{4}$$

where $t_{solid,min}$ is the minimum solidification time from all points in the 2D cross-section. Following this, the length of the melt pool front, L_F, is determined by evaluating the melting time of each coordinate, $t_{melt,yz}$, in the 2D cross-section:

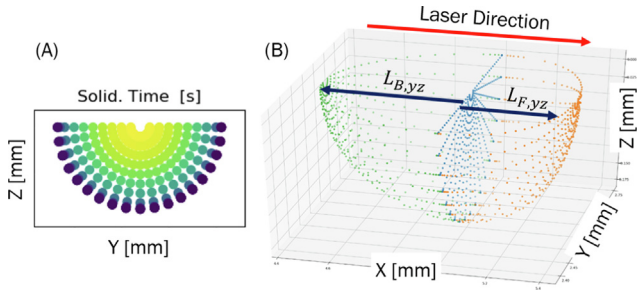

Fig. 2. Melt pool schematic. (A) YZ-melt pool extent (B) 3D melt pool projection.

$$L_{F,yz} = \left(t_{solid,min} - t_{melt,yz}\right)u \tag{5}$$

Fig. 2 (B) then illustrates the derived 3D melt pool, where length, width, and depth correspond to x, y, and z coordinates, respectively. These points may be represented as a convex hull, allowing the melt pool volume to be determined. It should be noted that the resolution of this convex hull is dependent on the number of 2D intermediary points considered. However, the calculation of additional points will increase computational cost and approach a diminishing return regarding the convex hull volume.

2.1.4. Keyhole depth correction

Our previous work [34] with similar analytical models showed that these models typically underestimate the melt pool depth for the print conditions with particular combinations of high laser powers and low laser velocities that correspond to the keyhole mode. In these cases, high linear energy density ($LED = \frac{P}{u}$) input from the laser beam and lack of time for the substrate to dissipate energy via heat diffusion mechanism across the material cause heat accumulation in the melt pool and a local rise in temperature above the material boiling temperature, inducing substantial elemental evaporation. This large evaporative effect imposes an opposite force on the melt pool surface, known as the recoil pressure, which results in deeper penetration of the molten material, considerably increasing the melt pool depth under these conditions [37]. Since the physics associated with the keyholing phenomenon is not considered in such analytical thermal models, the model response for depth is corrected for the print conditions experiencing keyholing, as proposed in [34]. This depth correction is performed based on a simplified model proposed by Gladush and Smurov [38], providing a general solution for keyhole depth, d. Derivation involves solving the heat conduction equation for a semi-infinite slab under the assumption of cylindrical keyhole formation with radius σ resulting from the laser beam interaction:

$$d_k = \frac{\eta P}{2\pi\kappa T_b}\ln\left(\frac{\sigma + \frac{D}{u}}{\sigma}\right) \tag{6}$$

where T_b is the boiling temperature.

The differences between the melt pool depths predicted by the thermal model and their experimental counterparts are assumed to be proportional to the formulation in Eq. 6 when the input variables fall into the keyholing regime. Therefore, a correction factor, C, multiplied with this formulation is added to the predicted depth for each print experiencing the keyholing regime. The probabilistic calibration of parameter C and other uncertain material properties in the thermal model against available experimental data for melt pool width, w_{exp}, and depth, d_{exp}, is discussed in Section 2.4. It should be noted that an experimentally-derived criterion [30,29], i.e., $\frac{w_{exp}}{1.5} \leqslant d_{exp}$, is considered in this parameter calibration to find

the experiments with the keyholing effect, where the depth correction is required to be applied in their corresponding model predictions. This keyholing criterion can also be used to identify the corresponding Power-Velocity region in the processing space of NiTi SMAs, which indicates whether or not a prediction needs the keyhole depth correction based on the print input conditions.

2.2. Experimental procedures

Gas-atomized $Ni_{51.2}Ti_{48.8}$ [at%] powder with $d80$ (the 80th percentile of the powder size distribution) of 32 μm provided by *Nanoval GmbH & Co. KG* is used to manufacture the single tracks in this work. Samples are printed using a 3D Systems ProX DMP 200 Laser Type (fiber laser with a Gaussian profile λ = 1070 nm, and a beam size (4σ) of 80 μm) with a powder layer thickness (q) of 30 μm ($\sim d80$). These single-track prints are performed on equiatomic NiTi substrates cut from larger cylindirical bars using wire electro-discharge machining (EDM). The printed single tracks are sectioned orthogonal to the direction of beam travel, and the cross sections are polished up to a 0.25 μm water-based diamond solution. They are then etched in one part HF, three parts HNO_3, and ten parts of DI water for 15 s to reveal the melt pool shape. Using optical microscopy (OM) images, the depth and width of melt pools are measured in three YZ-plane cross-sections in each single-track. Their averages, listed in Table 1, are utilized for the calibration and validation of the thermal model. In Fig. 3, some of the OM cross-section images are shown for prints performed at different laser powers and velocities, which result in different print modes during the LPBF process.

2.3. Calibration approach

An adaptive Markov Chain Monte Carlo (MCMC) procedure is applied to conduct Bayesian parameter inference. In this calibration framework, the prior belief (or distributions) for uncertain parameters are updated to their posterior distributions, given the available experimental data represented by a likelihood function. In this context, solving the intractable integrals for the statistical inference of parameters necessitates a sampling method. Pseudocode detailing this adaptive MCMC algorithm is shown in Fig. 4.

The process starts with an initial guess for the parameter values, represented by prior distributions, and then proceeds by the sequential sampling of parameter vectors from a proposal posterior distributions. In this work, the proposal distribution is considered a multivariate normal distribution centered at the previous parameter vector in the MCMC chain with a variance-covariance matrix adapted in each sampling iteration by the variance-covariance matrix of previous samples based on [39]. The parameter samples are accepted or rejected during the sequential process, using the Metropolis-Hastings criterion that accepts the new sample with a probability equal to min{MH,1} in each iteration. Here, MH is the Metropolis-Hastings ratio that compares the joint probability (prior*likelihood) of the new sample with the previous one in the chain, as well as the probability of moving from the previous to the new sample with the probability of the reverse move. If the new sample is rejected, the previous sample repeats in the chain. It should also be noted that the prior and likelihood were considered as uniform distributions and a multivariate normal distribution, respectively, centered at the independent experimental data with a constant diagonal variance-covariance representing the average

Table 1
Average measured melt pool width and depth for single-track prints, measured from $Ni_{51.2}Ti_{48.8}$ powder at different process conditions. Experimental measurements are separated for the thermal model calibration and validation.

P (W)	u (mm/s)	LED (J/m)	$\bar{w}$ (μm)	$\bar{d}$ (μm)
Experimental Data Used for Thermal Model Calibration				
40	80	500.0	135.11 ± 18.46	25.90 ± 8.67
80	330	242.4	129.65 ± 1.41	32.55 ± 1.91
120	580	206.9	101.52 ± 22.52	27.03 ± 5.48
200	580	344.8	149.26 ± 6.64	85.14 ± 8.65
120	830	144.6	101.84 ± 16.16	26.40 ± 6.87
160	830	192.8	112.10 ± 0.43	48.69 ± 8.30
240	830	289.2	136.52 ± 9.33	77.14 ± 8.92
160	1080	148.1	109.63 ± 19.63	16.49 ± 4.71
200	108	185.2	114.01 ± 11.52	37.37 ± 3.51
240	1080	222.2	115.92 ± 7.96	57.75 ± 5.92
200	1330	150.4	110.72 ± 15.83	24.77 ± 2.29
240	1580	151.9	107.96 ± 5.20	35.98 ± 3.26
60	205	292.7	114.23 ± 14.67	41.40 ± 8.99
60	455	131.9	78.70 ± 5.28	21.73 ± 4.38
100	455	219.8	117.06 ± 9.96	60.82 ± 17.78
160	80	2000.0	326.84 ± 0.68	376.65 ± 38.90
200	80	2500.0	377.51 ± 12.04	469.21 ± 53.69
240	80	3000.0	417.41 ± 20.31	511.68 ± 38.77
160	330	484.8	160.93 ± 5.71	139.49 ± 46.69
200	330	606.1	176.22 ± 12.650	207.64 ± 43.66
240	330	727.3	201.84 ± 21.32	283.93 ± 13.06
240	580	413.8	148.27 ± 8.40	195.40 ± 10.87
100	205	487.8	165.11 ± 5.88	119.60 ± 19.16
140	205	682.9	179.19 ± 5.30	251.66 ± 1.77
140	455	307.7	138.43 ± 4.95	140.13 ± 26.36
Experimental Data Used for Thermal Model Validation				
80	80	1000.0	230.79 ± 9.65	143.10 ± 11.58
160	580	275.9	124.06 ± 16.72	42.11 ± 20.77
200	830	241.0	126.04 ± 1.56	72.61 ± 6.65
240	1330	180.5	109.66 ± 3.49	32.60 ± 14.15
200	1830	109.3	61.39 ± 19.01	19.06 ± 10.08
240	1830	131.1	97.58 ± 4.13	40.86 ± 8.26
120	80	1500.0	291.66 ± 4.92	248.01 ± 15.73
120	330	363.6	138.36 ± 3.63	108.28 ± 7.01

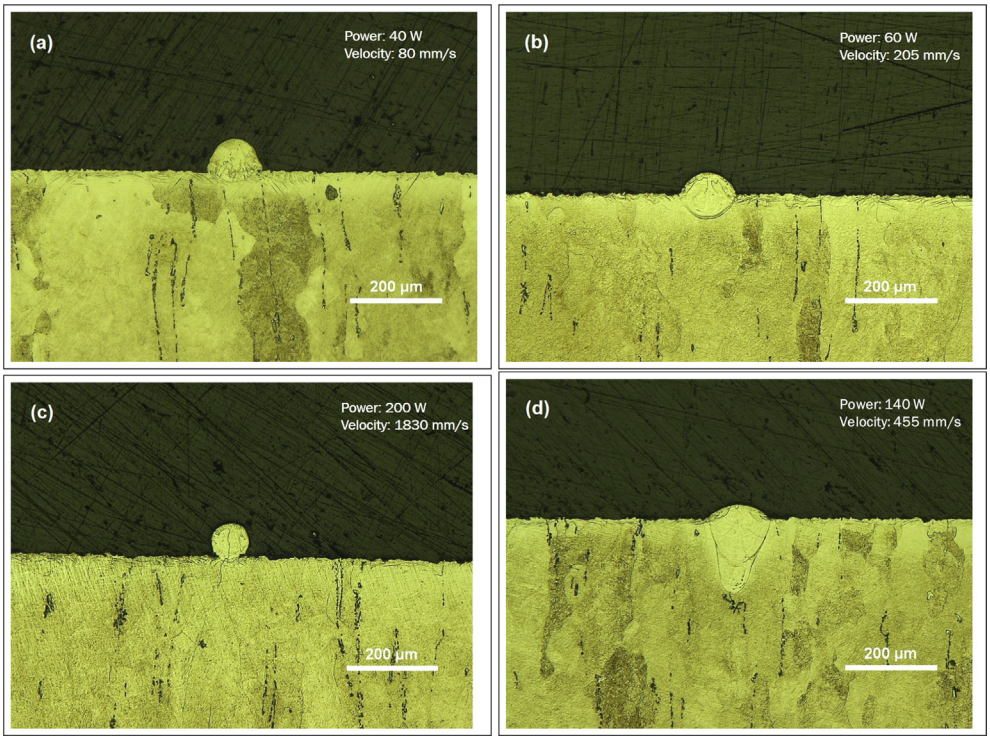

Fig. 3. Cross-section print images obtained from optical microscopy for different print conditions during the LPBF process, indicating different print modes, (a) lack of fusion, (b) good quality, (c) balling, and (d) keyholing modes.

experimental uncertainty for width and depth measurement. The mentioned sampling process stops when the proposal distribution reaches a stationary state as the parameter convergence occurs. At the end of this process, the samples before the parameter convergence, known as the burn-in period, are removed from the chain in order to represent the posterior frequency/probability distributions of model parameters and their statistical characteristics (see [41–47] for further details about the applied MCMC calibration approach).

2.4. Calibration results

Generally, all models are surrogates of reality with their specific assumptions and approximations, regardless of their fidelity and cost. Therefore, their probabilistic calibration against data is required in order to provide the most plausible predictions within their uncertainty bounds. It should also be noted that Bayesian calibration is not hindered by limited data, providing the best inference corresponding to the current state of knowledge. In this work, modeling of the melt pool geometry is one of the main components to the modeling of the print as a whole, emphasizing the importance of calibrating the thermal model. The DSM calibration is conducted using the results obtained from 33 single-tracks listed in Table 1 (split into 25 training and 8 test data points), printed using $Ni_{51.2}Ti_{48.8}$ powder, as described in Section 2.2. Melt pool widths and depths measured from these prints at different combinations of laser power and velocity are used simultaneously in a multi-objective optimization scheme, based on the adaptive MCMC described in Section 2.3, to provide a probabilistic estimation of the model parameters. The calibration parameters are then η, effective κ, effective C_P, and C, while other parameters remained constant. Additionally, by utilizing data from both conduction and keyhole regions, the model is effectively homogenized for both modes through the calibrated model parameters and any uncertainties related to this are covered in the uncertainty quantification.

After generating 20,000 MCMC samples for the mentioned parameters and removing the burn-in period, the marginal probability density functions (PDFs) were plotted for each parameter in Fig. 5. The average and standard deviations of these parameter samples were also reported in Table 2, representing the parameter plausible optimal values and uncertainties. As shown in Fig. 6, the correlation between parameter pairs can also be studied qualitatively and quantitatively through the 2D joint PDF plots and the Pearson linear coefficient, $\rho_{X,Y} = \frac{cov(X,Y)}{\sigma_X \sigma_Y}$, respectively. In the plots in Fig. 6, the colors represent the density of parameter samples in the joint parameter spaces, and the linearity of color features qualitatively demonstrates the degree of linear correlation between each parameter pair. The Pearson linear correlations, ρ, shown at the bottom right corner of each plot can change from -1 to 1, with a value close to -1 or 1 indicating strong correlation and a value close to 0 indicating weak correlation between the parameters. It is worth noting that the negative and positive signs show the correlation direction. Here, the ρ values suggest a strong correlation between the thermal model parameters. This can be expected due to the linear correlation between heat capacity and thermal conductivity [48] and due to the efficiency parameter acting as a tuning metric. Additionally, a very weak correlation is seen between the thermal model parameters and C, implying an independent effect of parameter C and its non-substitutability with the other three parameters. These correlations help explain a trend observed in Fig. 5, where the probability for η increases as the upper bound is approached, implying a peak value greater than 0.8. However, this high efficiency is physically impossible, and could be a result of the missing physics in the model and the uncertainties in the experimental measurements. Addressing these issues in future work would then allow the posterior peak for η to shift to a reasonable range for this parameter. Two other model parameters observe similar trends due to their high linear correla-

Algorithm 1: Adaptive MCMC algorithm used in this work

input:

- Initial guess for parameters $\boldsymbol{\theta}^0$, lower bounds $\boldsymbol{\theta}_{min}$, upper bounds $\boldsymbol{\theta}_{max}$, prior density $p(\boldsymbol{\theta})$, and number of samples N_s
- Data $\boldsymbol{D} \leftarrow \{\boldsymbol{D}^k\}_{k=1}^K$ and a diagonal variance-covariance matrix fixed for all data $\boldsymbol{\Sigma}_{\boldsymbol{D}^k} \leftarrow \boldsymbol{\Sigma}_{\boldsymbol{D}}$
- Initial guess for the proposal variance-covariance matrix $\boldsymbol{\Sigma}^0$

output:

- Generated samples $S = \{\boldsymbol{\theta}^0, \ldots, \boldsymbol{\theta}^{N_s}\}$ and posterior density of the parameters $p(\boldsymbol{\theta}|\boldsymbol{D})$

Initialize

$S \leftarrow \emptyset$

for $i \leftarrow 1$ to N_s do

  if $i = 1$ then

    $q(\boldsymbol{\theta}|\boldsymbol{\theta}^0) \leftarrow \mathbb{N}(\boldsymbol{\theta}^0, \boldsymbol{\Sigma}^0)$

  else

    Adapt the proposal posterior density:

    $q(\boldsymbol{\theta}|\boldsymbol{\theta}^{i-1}) \leftarrow \mathbb{N}(\boldsymbol{\theta}^{i-1}, \boldsymbol{\Sigma}^{i-1})$ s.t. $\boldsymbol{\Sigma}^{i-1} \leftarrow S_d[\boldsymbol{\Sigma}^{i-2} + \varepsilon I_d], S_d \leftarrow \frac{2.4^2}{d}$, and $\varepsilon > 0$

  end if

  Draw a candidate from the proposal posterior density: $\boldsymbol{\theta}^{cand} \sim \mathbb{N}(\boldsymbol{\theta}^{i-1}, \boldsymbol{\Sigma}^{i-1})$

  Calculate Metropolis-Hastings ratio:

  $MH \leftarrow \frac{p(\boldsymbol{\theta}^{cand})p(\boldsymbol{D}|\boldsymbol{\theta}^{cand})}{p(\boldsymbol{\theta}^{i-1})p(\boldsymbol{D}|\boldsymbol{\theta}^{i-1})} \frac{q(\boldsymbol{\theta}^{i-1}|\boldsymbol{\theta}^{cand})}{q(\boldsymbol{\theta}^{cand}|\boldsymbol{\theta}^{i-1})}$ s.t. likelihood $p(D|\theta) \leftarrow \prod_{k=1}^K \mathbb{N}(\boldsymbol{D}^k, \boldsymbol{\Sigma}_{\boldsymbol{D}})$

  Draw a random number from a uniform distribution in the range of 0 to 1: $u \sim \mathrm{Unif}[0, 1]$

  if $MH > u$ then

    Accept the candidate: $\boldsymbol{\theta}^i \leftarrow \boldsymbol{\theta}^{cand}$

  else

    Reject the candidate: $\boldsymbol{\theta}^i \leftarrow \boldsymbol{\theta}^{i-1}$

  end if

  Update the sample chain: $\boldsymbol{S} \leftarrow \boldsymbol{S} \cup \{\boldsymbol{\theta}^i\}$

end for

Remove the burn-in period: $\boldsymbol{S}_{post} \leftarrow \boldsymbol{S} - \boldsymbol{S}_{burn}$

Determine the parameter posterior density: $p(\boldsymbol{\theta}|\boldsymbol{D}, \boldsymbol{S}_{post})$

Fig. 4. Pseudocode describing the implementation of the adaptive MCMC algorithm.

tion with η, κ with ρ = 0.93 and more prominently in C_P with ρ = 0.99. However, as an extrinsic factor, C can independently peak around an optimal value due to its low linear correlation with the other parameters.

The mean values and uncertainties of the parameters in Table 2 were propagated to the model outcomes used for the calibration, i.e., melt pool width and depth, using forward model analysis. In this uncertainty propagation (UP) method, the MCMC converged samples are run through the model with the keyhole depth correction to obtain the corresponding output samples for melt pool width and depth. Then, 2.5% of the samples are removed from both ends of the sorted output samples to find 95% credible intervals for each output. Fig. 7 shows the comparison between the calibrated model results and their corresponding experimental data for each training- and test-experimental conditions. In this figure, colors indicate *LED* values. In part (a) and (b) of this figure, it can be observed that there is excellent agreement between the mean values for the calibrated model results and training-experimental measurements, as deduced from high R^2 values of 0.97 and low RMSE values less than 25 μm. The comparison results for test-experimental conditions in part (c) and (d) also imply good validation of the calibrated model. Therefore, despite missing physics in the model and uncertainties in the experimental data, the calibrated thermal model, utilizing mean parameter values reported in Table 2, can be used in Section 3 to estimate the evaporation flux and final composition of the matrix after the multi-track multi-layer prints at different process conditions. In this regard, it should be noted that changes in the calibrated material properties due to the change in powder composition from 51.2 to 50.8 Ni [at%] in Section 3 are small and can be ignored.

3. Predicting location-specific composition

Illustrated in Fig. 8, user input, consisting of process parameters and material properties, informs the hierarchical model, enabling chemistry predictions across an AM part. The chemistry of the part can then be linked to properties and performance. The resolution of this hierarchical chain, also known as the forward problem, is an essential task in design under the ICME scheme.

3.1. Multi-layer model

The Multi-Layer Model (MLM) enables part-level simulation of the LPBF AM process by utilizing thermal history and geometric relations to replicate the build from the substrate up. In a Cartesian coordinate system, the MLM constructs a 2D slice projected into

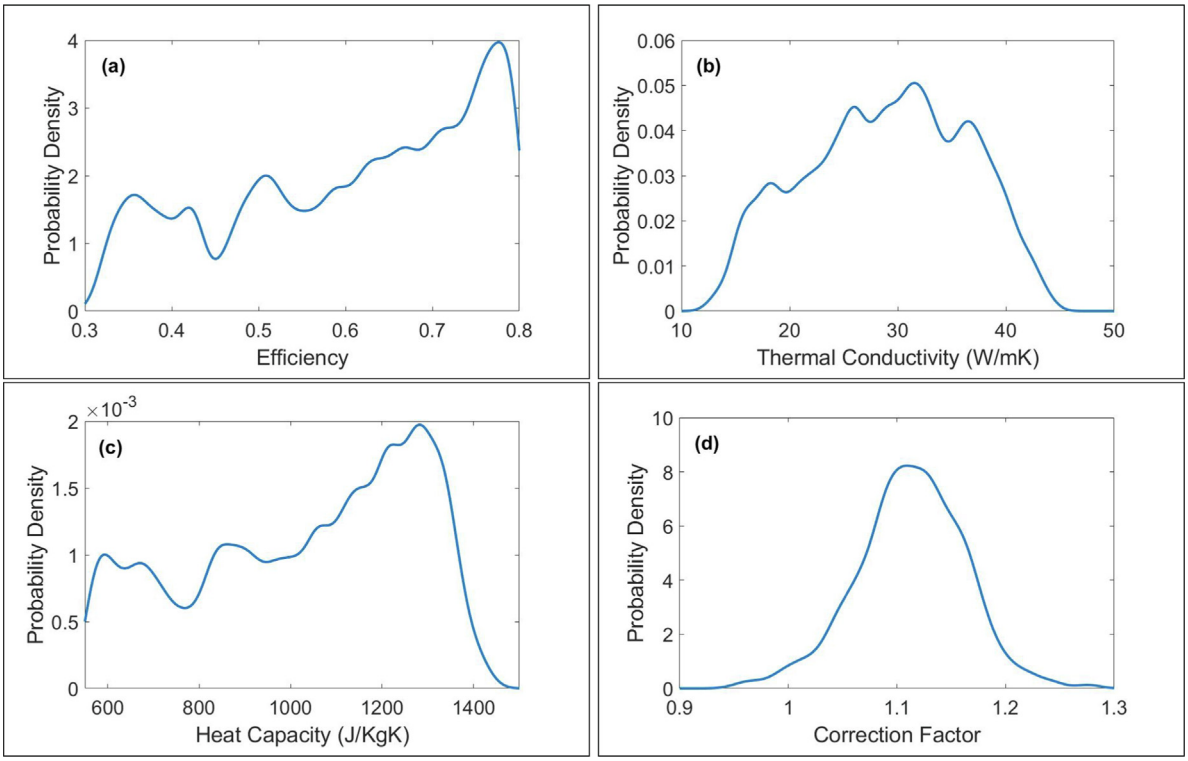

Fig. 5. Marginal posterior density functions of parameters in the DSM thermal model after the MCMC-Bayesian calibration with $Ni_{51.2}Ti_{48.8}$ SMA single-track experiments.

Table 2
MCMC-Bayesian calibrated parameters in the DSM thermal model: mean values and one standard deviation of MCMC samples after removing the burn-in period.

η	κ (W/m K)	C_p (J/kg K)	C
0.61 ± 0.14	28.9 ± 7.3	1033.6 ± 243.6	1.11 ± 0.05

3D. The DSM generates melt pool cross-sections along the YZ-plane for multiple tracks and layers, and melt pool lengths are projected in the x-direction to determine melt pool volume. Additionally, if the keyhole depth correction criteria is met, as discussed in Section 2.1.4, adjusted melt pool depths will be utilized by the MLM. Based on processing conditions, portions of each track and layer can also be categorized into steady-state and dynamic regions. In the case of a conventional hatching scan strategy with constant processing parameters and sufficient length, a melt pool generated in the center of a track, a steady-state region, could be extended in either direction to represent the entire steady-state region. However, regions where the process may be more dynamic, such as near the start or end of a track, could have a different thermal history than a steady-state region and should have separate MLM predictions generated. Through the MLM, a 2D slice across the cross-section of multiple tracks and layers in the steady-state region could then represent a substantial portion of the 3D AM part. Additionally, the MLM retains chemistry information for every point within the simulated 3D projection, enabling location-specific chemistry to be predicted and tracked through time, further aiding in location-specific property predictions across the part.

3.1.1. Assumptions

Modeling the AM process on a part-level can be taxing on resources, but is necessary for an accurate translation to part properties. In this regard, several assumptions are made in the MLM to improve computational efficiency and retain adequate resolution. These assumptions and their corresponding justification are expressed below; this is proceeded by a more detailed discussion.

1. The intralayer preheat effect is automatically captured by the DSM and drives changes in melt pool dimensions from one track to the next. However, once the difference in dimensions of the current and previous track reaches the desired tolerance, i.e., 10*e*-15 μm, it is assumed that these steady-state melt pool dimensions can be applied to the remaining tracks in the print layer for the sake of reducing computational cost. This approach could be revised based on scan strategy.
2. The interlayer preheating is assumed to be constant for all layers deposited due to previous experimental work [36,49] showing homogeneity within an AM part at different print layers, confirming there is sufficient time between layers to reduce preheating effects in our experiments. However, in the case that preheating is significant, it can be implemented in the DSM by adjusting the parameter for background temperature.
3. If the melt pool overlap formed by track N and an adjacent track is sufficiently small, e.g., less than 1% cross-sectional area overlap, the chemistry propagation is considered negligible.

In the case of a single-layer with multiple tracks, the diffusion of heat from one track acts as a preheat for adjacent tracks. This results in a slight variation in melt pool size, affecting several tracks depending on part geometry and process parameters before steady-state dimensions are reached. In the steady-state regions, thermal history, respective melt pool geometry, and melt pool overlap remain approximately constant. Due to this symmetry, a single melt pool can be projected along the steady-state length of a track. The MLM implemented in this study utilizes individual melt pool geometry from the first track until steady-state, whereafter the remaining melt pool dimensions have equivalent dimensions, allowing several melt pools to model an entire layer. Additionally, preheating effects between layers are not considered.

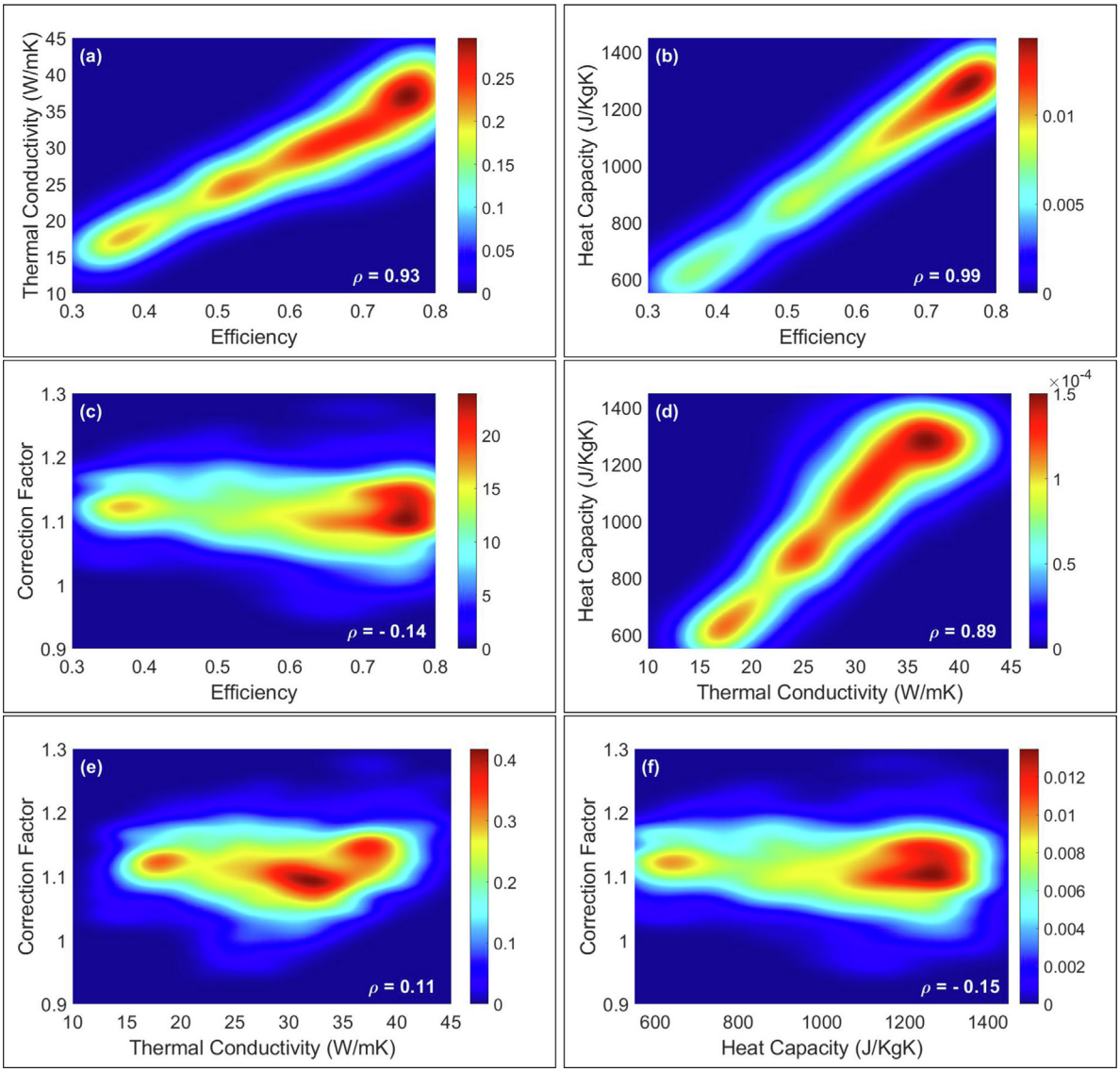

Fig. 6. Joint posterior density functions of parameter pairs in the DSM thermal model after the MCMC-Bayesian calibration with $Ni_{51.2}Ti_{48.8}$ SMA single track experiments. ρ represents the Pearson linear correlation.

This means that melt pool dimensions in each layer are identical to corresponding tracks in the previous layer, and a single layer can be used to model all build layers. Consequently, the steady-state region of the print can be modeled with several melt pools and a significant reduction in computational cost. Furthermore, the cross-sectional area of melt pool overlap with adjacent tracks varies based on processing parameters and intralayer preheating. As the overlap area decreased, the chemistry propagation between the melt pools also decreases. When a melt pool overlap region is sufficiently small, this effect becomes negligible. This simplification aids in reducing the number of melt pool overlaps that need to be evaluated for determining chemistry propagation, through each track and layer. Melt pool overlap is discussed in greater detail in the following section.

3.1.2. Melt pool overlap

The MLM provides insight on the chemistry propagation throughout a part by constructing the sample from the substrate up and tracking composition for every track and layer. The average composition of each melt pool is calculated based on overlap with melt pools from previous tracks in the same layer, and overlap with tracks in previous layers and/or the substrate. Fig. 9 illustrates this general relationship between melt pools on adjacent tracks and layers.

In the simplest scenario, Case A, the first melt pool corresponds to the first layer and first track of the build, MP_{L1T1}. This melt pool has an average composition, χ_{L1T1}, given by the volume fraction of powder, $V_{p,L1T1}$, with composition χ_p, and the volume fraction overlap with the substrate, $V_{Ovlp,L1T1|s}$, with composition χ_s. Here, layer thickness is used to define the boundary between the powder and substrate region. Case B then introduces the second melt pool of layer 1, MP_{L1T2}, which overlaps with MP_{L1T1} and the substrate. At this point in time, the entire length of the first track has been processed, meaning the volume encompassed by maximum cross-sectional overlap of MP_{L1T2} with MP_{L1T1} is represented by the volume fraction $V_{Ovlp,L1T2|L1T1}$ having composition χ_{L1T1}. Now, the overlap of MP_{L1T2} with the substrate, $V_{Ovlp,L1T2|s}$, not contained within $V_{Ovlp,L1T2|L1T1}$ must be determined. This can be achieved through Eq. 7.

$$V_{Ovlp,L1T2|s} \leftarrow V_{Ovlp,L1T2|s} - \left(V_{Ovlp,L1T2|s} \cap V_{Ovlp,L1T2|L1T1}\right) \tag{7}$$

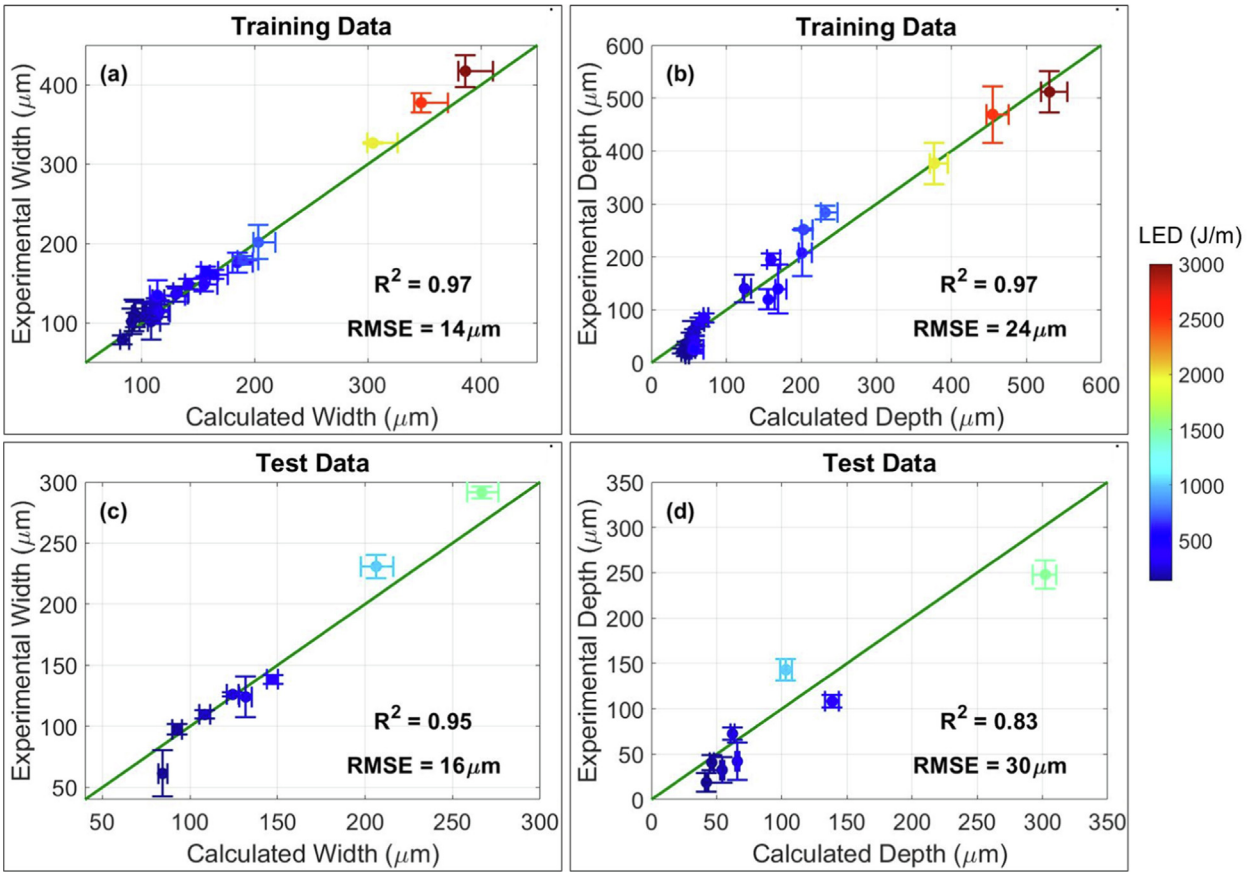

Fig. 7. Calibrated model predictions vs. experimental data for the melt pool width and depth produced during the single-track prints of the given $Ni_{51.2}Ti_{48.8}$ SMA. Colors indicate the LED values based on the given experimental input conditions.

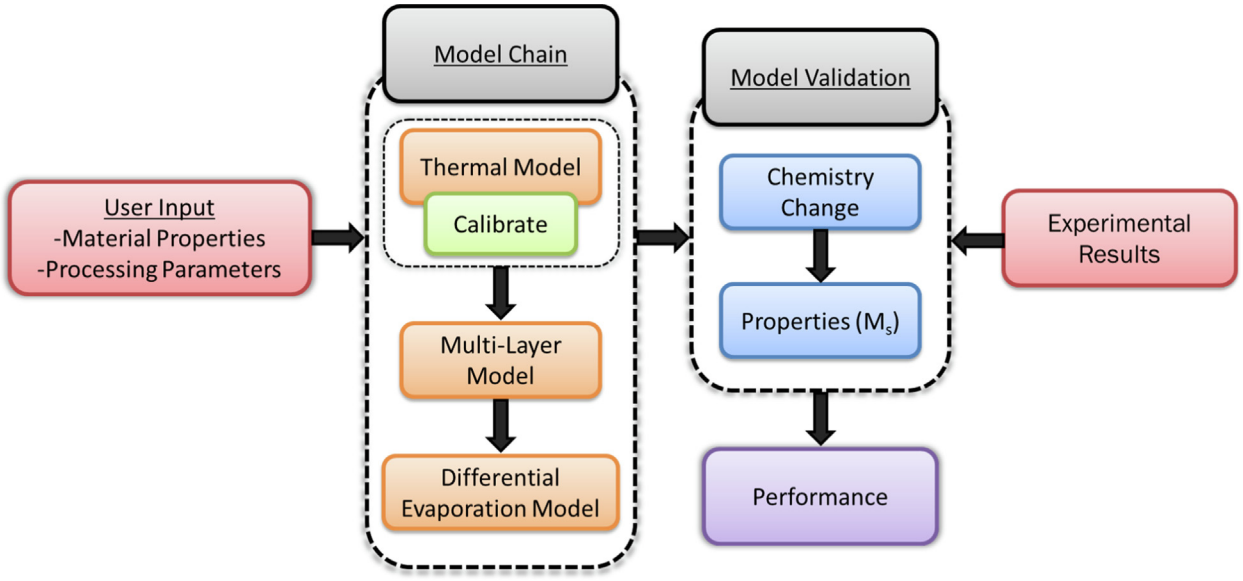

Fig. 8. Model methodology. User input is fed into the model chain comprised of the calibrated thermal model, the multi-layer model, and the differential evaporation model. This is followed by model validation with experimental results to determine location-specific chemistry and properties, and ends with an evaluation of performance.

Here, the intersecting region of the substrate overlap with $V_{Ovlp,L1T2|L1T1}$ is removed from $V_{Ovlp,L1T2|s}$ to redefine the volume fraction overlap of the substrate with MP_{L1T2}. The overlap and powder volume fractions and corresponding compositions are then used to determine the average composition of MP_{L1T2}, χ_{L1T2} . When considering a conventional snake scan strategy, and constant processing parameters, this procedure for calculating melt pool volume fraction and composition can be extended for the remainder of tracks in the first row. Even though the build process could result in a melt pool overlapping with multiple tracks, it is important to recognize the development of a time hierarchy, where the most recent event in time would be the influencing track. This means

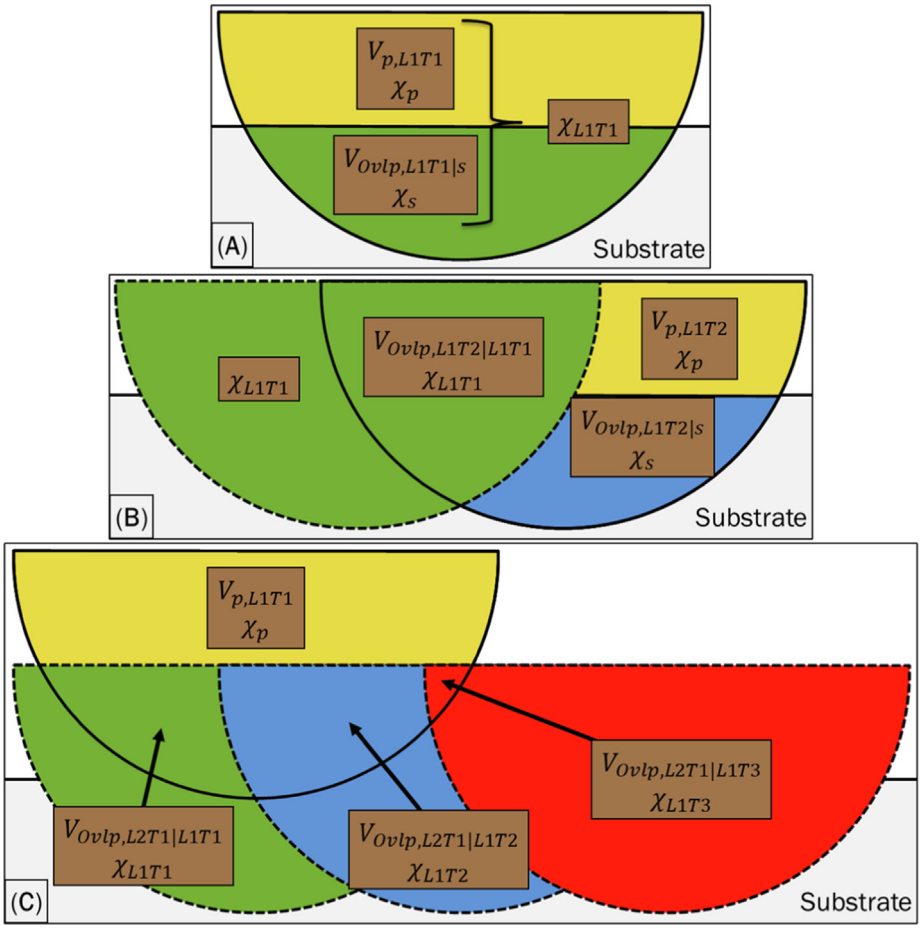

Fig. 9. Melt pool overlap and chemistry propagation general relationship. The terms are as follows: V - volume, χ - composition, p - powder, s - substrate, $Ovlp$ - overlap, L - layer, T - track, | - 'with'.

that, for any track in the first layer, $L1TN$, it is only necessary to consider overlap with the most recent adjacent track, $V_{Ovlp,L1TN|L1TN-1}$ and substrate, $V_{Ovlp,L1TN|s}$.

Case C follows a similar procedure, but there is added complexity in accounting for overlap with multiple melt pools in a previous layer instead of a constant substrate with constant composition. However, as with same-layer track overlap in a conventional snake scan strategy with constant processing parameters, multi-layer overlap is handled on a time hierarchy. Even though there might be overlap extending through several layers, the only necessary layer overlap to consider is with the layer directly preceding the current position. For MP_{L2T1}, this means consideration of the powder, $MP_{L1T3}, MP_{L1T2}, MP_{L1T1}$, and their respective volume fraction and composition. $V_{Ovlp,L2T1|L1T3}$ can be determined directly, however $V_{Ovlp,L2T1|L1T2}$ and $V_{Ovlp,L2T1|L1T1}$ require an adjusted application of Eq. 7. This process can become increasingly complex depending on process parameters, with the number of overlaps and overlap volume fraction strongly dependent on power, velocity, hatch, layer thickness, and material properties. This directly affects the chemistry propagation through the tracks and layers of the simulated part determined by the MLM. However, another important factor affecting composition and warranting consideration is the evaporation of material from the melt pool.

3.2. Differential evaporation model

The differential evaporation model (DEM) serves to account for the loss of material due to evaporation during the printing process and provide increased accuracy in predicted compositions. The DEM takes direct input from the thermal model, generates a melt pool, and applies a formulation for evaporation to account for material loss and provide an evaporation adjusted predicted chemistry. When utilizing the MLM, the average initial chemistry of each melt pool is fed into the DEM and the resulting chemistry fed back to the MLM. This linkage fully incorporates the effect of evaporation across the simulated sample and predicts chemistry resulting from the culmination of geometric and evaporation effects.

3.2.1. Assumptions

The development of the DEM begins with the generation of assumptions, for both the DSM (mentioned in Section 2.1) and DEM, used to describe and simplify the involved physics. Equations are formulated, encompassing these physics, to solve for differential evaporation and to predict chemistry. Assumptions for the DEM include:

1. The melt pool follows a mass balance.
2. There is complete mixing within the melt pool.
3. The Kinetic Theory of gases can be applied.

The implications of these assumptions are a solution to the mass flow in and out of the system, a spatially uniform composition of the melt pool, and an evaporation rate formulation derived from the Kinetic Theory of Gases, which itself is built on two postulates [50]:

1. Matter is composed of extremely small molecules, where molecules of the same chemical substance are facsimiles

2. Molecules of a gas are in constant motion → intimately related to temperature

3.2.2. Mass balance

A derivation for mass balance in a control volume was conducted, providing a formulation for chemistry change in a melt pool. Fig. 10 depicts the mass flow, in and out, of a melt pool in a control volume, whereby mass loss due to evaporation occurs through the melt pool surface, liquid-vapor interface.

The following relation describes the mass flow through the control volume:

$$\dot{m}^{out} = \dot{m}^{in} - \dot{m}^{evap} \tag{8}$$

where $\dot{m}^{in}$ [kg/s] is the mass flow rate into the melt pool, $\dot{m}^{out}$ [kg/s] is the mass flow rate out of the melt pool, and $\dot{m}^{evap}$ [kg/s] is the mass flow rate, due to evaporation, out the top surface of the melt pool. Here, $\dot{m}^{in}$, $\dot{m}^{out}$, and $\dot{m}^{evap}$ are expressed, respectively, as:

$$\dot{m}^{in} = \int_{in} \rho\left(\vec{u}\cdot\hat{n}\right)dA \tag{9}$$

$$\dot{m}^{out} = \int_{out} \rho\left(\vec{u}\cdot\hat{n}\right)dA \tag{10}$$

$$\dot{m}^{evap} = \sum_{iso=1}^{n}\int_{top} j(\chi_A,\chi_B,\ldots,T_{iso})dS_{iso} \tag{11}$$

where ρ is the density of mass moving in a velocity field $\vec{u}\cdot\hat{n}$ perpendicular to the cross-sectional area of the control volume (defined as the extent of the melt pool) dA, and j is the evaporation flux, dependent on the chemistry of the alloying elements $(\chi_A,\chi_B,\ldots)$ and the temperature of interest (T_{iso}), out of the isotherm area (dS_{iso}) corresponding to the temperature of interest. The evaporative flux is a continuous function of both the alloy composition and the temperature. The latter varies spatially across the liquid-vapor interface. To simplify the integral we discretize the liquid-vapor interface into several regions bounded by selected isotherms and assume uniform temperature within each of these subdomains. It should be noted that the boiling isotherm accounts for a majority of the mass loss due to evaporation in the melt pool. Eqs. 9 and 10 are reduced to:

$$\dot{m}^{in} = \rho^{in}\omega^{in}uA^{in}_{x-s} \tag{12}$$

$$\dot{m}^{out} = \rho^{out}\omega^{out}uA^{out}_{x-s} \tag{13}$$

where $\rho*\omega$ $[\mathrm{kg/m^3}]$ represents the density of the alloy multiplied by the alloying element's weight fraction, and A_{x-s} $[\mathrm{m^2}]$ is the front projected area of the melt pool.

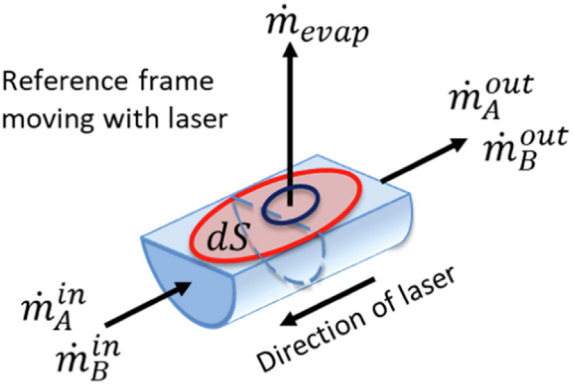

Fig. 10. Mass balance of a melt pool in a control volume. This includes mass flow in, mass flow out, and mass loss due to evaporation.

If the melt pool is thoroughly mixed, we can then assume that the liquid has a spatially uniform composition, the chemistry of the alloying elements can be considered constant. As a result, Eq. 11 becomes:

$$\dot{m}^{evap} = \sum_{iso=1}^{n} j(\chi_A,\chi_B,\ldots,T_{iso})S_{iso} \tag{14}$$

From here, the mass balance (Eq. 8) may be re-written as a first-order steady-state solution for each alloying element i by substituting Eqs. (12)–(14):

$$\dot{m}_i^{out} = (\rho_i^{in}*\omega_i^{in})uA^{in}_{x-s} - \sum_{iso=1}^{n} j_i(\chi_A,\chi_B,\ldots,T_{iso})S_{iso} \tag{15}$$

3.2.3. Evaporation Rate

The DEM follows a sequence of several calculations, completed for each alloying element (Ni and Ti in NiTi), to predict the chemistry at a location in an AM part:

1. Calculate Equilibrium Vapor Pressure, as a function of isotherm temperature and incoming chemistry.
2. Determine Evaporation Rate, according to Eq. 18.
3. Conduct Mass Balance, as described in Eq. 15.

In order to calculate the equilibrium vapor pressure, $\bar{p}_i$ $[atm]$, the standard pressure of the alloying element, p_i° $[atm]$, must first be evaluated. This was accomplished through Antoine's equation (Eq. 16), derived from the Clausius-Clapeyron relation, where A, B, and C are Antoine coefficients, listed in Table 3, and T $[^{\circ}C]$ is the temperature of interest [51]:

$$p_i^{\circ} = 10^{\left(A-\frac{B}{C+T}\right)/760} \tag{16}$$

The equation for equilibrium vapor pressure, for each alloying element, is then:

$$\bar{p}_i = p_i^{\circ}a_i \tag{17}$$

where a_i is the activity of the respective alloying element. Activity values were generated through Thermocalc 2020b TCHEA4 database for temperatures ranging from T_{melt}-T_{boil} for a desired composition. The evaporation rate for each element is then determined through the Kinetic Theory of Gases as:

$$j_i = 44.331\bar{p}_i\left[\frac{M_i}{T}\right]^{\frac{1}{2}} \tag{18}$$

where j_i [g/(cm^2 s)] is the vaporization rate of species i, $\bar{p}_i$ $[atm]$ is the equilibrium vapor pressure of i, M_i [g] is the molecular weight of i, and T [K] is the absolute temperature. This is followed by the mass balance (Eq. 15) for each alloying element. From the mass balance, the mass flow out of the melt pool can be related to the weight fraction of Ni and Ti along with the melt pool's updated chemistry. This procedure is repeated for multiple melt pools, based on scan strategy and sample size, to consider cumulative thermal effects from adjacent layers and tracks on the location-specific chemistry prediction of the AM part.

The model took a quick and simple approach to chemistry prediction, utilizing the thermal history of a designated point of interest. This thermal history was segmented based on the number of desired

Table 3
Antoine coefficients for Ni and Ti [51].

Element	A	B	C
Ni	−8.75	17882.38	134.99
Ti	8.90	20948.99	190.76

isotherms, with surface area and interaction time calculated for each. The mass balance was resolved and chemistry predicted.

3.3. Experimental procedure

For the validation of the DEM, gas atomized $Ni_{50.8}Ti_{49.2}$ [at%] powder with a $d80$ of 38 μm was used to fabricate $10 \times 10 \times 10$ mm^3 cubes. As shown in Table 4, the laser power and scanning velocity were in the range of 60–240 W and 80–1330 mm/s, respectively. The Oxygen level in the print chamber during printing and the layer thickness were 500 ppm and 40 μm, respectively. The volumetric energy density ($VED = \frac{P}{uhL_t}$, where h is hatch distance and L_t is layer thickness) for these 21 cube prints vary from 52.9 to 234.4 J/mm^3.

A differential scanning calorimetry (DSC) sample of the powder was solution heat-treated at 950 °C for 1 h under protective argon atmosphere in order to determine the transformation temperatures of the powder in single phase (without any precipitates which may change the transformation temperatures and the matrix composition). In addition, DSC samples with 3 mm diameter and 1 mm thickness were cut from the printed cubes using wire EDM, and then solution heat-treated at 800 °C for 1 h in argon, again in order to eliminate any second phases, residual stresses or any other microstructural features that may affect the transformation temperatures. This is critical because the Ni content of the prints are indirectly determined using the transformation temperatures, as explained in the following section in detail. A TA Instruments Q2000 DSC is used to measure the transformation temperatures of both powder and the printed cubes. Two thermal cycles were performed during the DSC measurement at a heating/-cooling rate of 10 °C/min between −150 °C and 150 °C, and the transformation temperatures listed in Table 4 were extracted from the second cycle using the intersecting tangent method [52]. These transformation temperatures include martensite start temperature, M_s, martensite finish temperature, M_f, austenite start temperature, A_s, and austenite finish temperature, A_f. The following section will focus on M_s, however, a similar procedure could be used for the remaining transformation temperatures.

3.4. Nickel content and martensitic transformation temperature (M_s)

In NiTi SMA literature, it is well-known that determining the exact Ni content of Ni-rich NiTi SMAs at the desired level of accuracy is very challenging, if not impossible, using known chemistry measurement techniques [9,53,54]. This is due to the extreme sensitivity of martensitic transformation temperature to the Ni content in materials with Ni contents greater than 50 at% as shown in Fig. 11. Such chemical sensitivity requires the determination of Ni content on the order of 0.01 at% level in bulk samples. As seen in Fig. 11, there are two distinct regions defined by the M_s-Ni relationship, where M_s is the martensite start temperature. At Ni contents less than ~49.8 at%, M_s remains relatively constant, while a strong negative trend is seen with Ni content greater than ~49.8 at%. This negative slope becomes larger as the Ni content approaches 51 at%, and corresponds to a change of over −100 [K/Ni at%]. This demonstrates a strong sensitivity of M_s to Ni content in the NiTi system, and reinforces the importance for accurately predicting composition to tailor location-specific properties. Therefore, in the present study we used the measured M_s temperatures to calculate the Ni content of the printed samples as described below and compare these with the Ni contents predicted using the DEM.

Nickel content is determined from the M_s temperature attained through DSC by utilizing an empirical relation for Ni [$at\%$] and M_s [K] [9]:

$$M_s(\chi_{Ni}^T) = (A + B * \chi_{Ni}^T) + C * D^{(\chi_{Ni}^T - 50)} \tag{19}$$

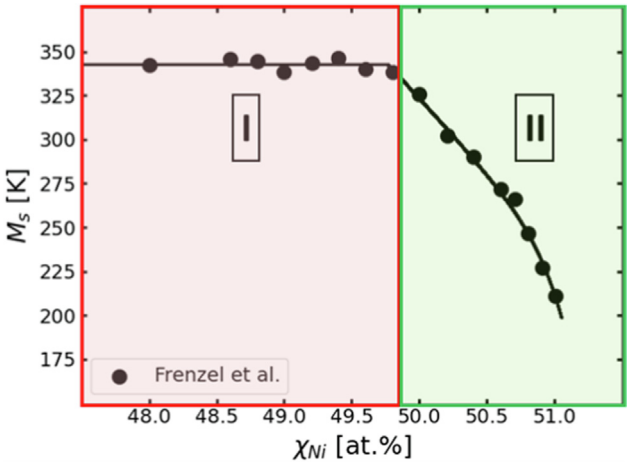

Fig. 11. Nickel content and corresponding M_s for multiple NiTi samples. Data from Frenzel et al. [9] Region I: Non-Invertible, Region II: Invertible.

Table 4
Process parameters and the transformation temperatures after solution heat treatment for the 21 cubes manufactured from $Ni_{50.8}Ti_{49.2}$ powder.

P (W)	u (mm/s)	h (μm)	LED (J/mm)	VED (J/mm^3)	M_s (°C)	M_f (°C)	A_s (°C)	A_f (°C)
160	1080	70	148.1	52.9	−19.81	−33.29	−3.46	9.37
65	297	100	218.9	54.7	11.23	−18.81	9.81	41.40
240	1330	80	180.5	56.4	−22.9	−29.21	−1.11	11.17
200	1080	80	185.2	57.9	−23.61	−36.61	−6.39	7.44
160	830	80	192.8	60.2	−18.62	−29.62	−2.61	9.37
200	830	100	241.0	60.2	−27.70	−35.90	−6.33	3.94
160	580	110	275.9	62.7	−18.75	−27.66	−1.16	11.09
120	330	130	363.6	69.9	3.81	−10.56	16.27	32.00
80	330	80	242.4	75.8	12.78	−4.05	22.83	42.34
96	297	100	323.2	80.8	15.10	−5.24	24.25	44.40
65	200	100	325.0	81.3	27.35	10.62	37.61	57.34
96	350	80	274.3	85.7	21.93	−3.65	26.51	50.25
60	160	100	375.0	93.8	38.59	19.17	47.52	70.19
96	250	100	384.0	96.0	20.95	1.87	34.24	51.24
96	297	80	323.2	101.0	21.37	−8.47	20.25	51.14
96	200	100	480.0	120.0	32.58	14.93	43.76	62.63
60	120	100	500.0	125.0	54.38	33.13	63.39	86.45
72	120	120	600.0	125.0	47.57	28.31	57.42	79.42
60	80	120	750.0	156.3	66.79	44.49	78.19	99.79
65	80	120	812.5	169.3	69.95	48.12	81.97	102.83
60	80	80	750.0	234.4	70.76	52.97	89.74	106.25

where M_s [K] is the martensite start transformation temperature, A is 4511.2373, B is −83.42425, C is −0.04753, D is 204.86781, and χ_{Ni}^{T} is the true Ni content [at%].

4. Model validation results and discussion

Following the previously stated methodology, the combined DSM-MLM-DEM was used to model the printing process of the 21 solution heat treated (SHT) 50.8 Ni [at%] samples (mentioned in Section 3.3) and predict Ni content after the thermal process. Pertaining to the DSM, relevant input parameters are listed in Table 5. Additionally, the surface area of each melt pool was binned into 5 equally spaced isotherms, spanning NiTi's melting to boiling temperature (1312–3187 °C), for the application of the DEM.

Fig. 12 compares the predicted Ni [at%] for each of the 21 SHT samples with the Ni [at%] derived from experiments. The data is divided into two regions based on the M_s and Ni relationship described in Section 3.4 and Fig. 11. In Region I, the experimentally derived Ni values reach a limit of approximately 49.8 [at%]. This is expected due to the non-invertible relationship of calculating Ni content from M_s, when M_s is approximately 335 K or higher. However, the combined DSM-MLM-DEM is not limited by this conversion, and directly calculates Ni compositions that may dip below this 49.8 [at%] threshold. This is demonstrated by several points in Region I with the predicted Ni [at%] below 49.8. Unlike Region I, the invertible relationship of calculating Ni content from M_s can be used in Region II. Both empirical and predicted Ni values are superimposed on a 45-degree line, demonstrating over- and under-predicting values that result from a combination of errors corresponding to the lack of knowledge about the parameters, possible missing physics or assumptions in DSM-MLM-DEM, and experimental measurements. Due to the non-invertible nature of Region I, only points located in Region II were considered in calculating the RMSE of 0.25 Ni [at%] and the Pearson correlation, ρ_{Ni}, of 0.85, suggesting a strong positive linear correlation between model predictions and experiment values. This means that the hierarchical DSM-MLM-DEM approach is capable of predicting Ni content in a range *well within the uncertainty of ±0.5 [at%]* for some of the chemistry measurement techniques such as wavelength dispersive spectroscopy (WDS) and inductively coupled plasma atomic emission spectroscopy (ICP-AES), and composition predictions followed expected trends, even in Region I. It should be noted here that although ICP-AES can be accurate to parts per million ranges for low-level constituents, the accuracy can be as low as ±2% of the absolute value for the major constituents [55]. It is also important to note that the predictions were achieved with only a calibrated analytical thermal model being fed to the MLM and DEM, which can be much faster than numerical thermal models (e.g. finite element models).

Predicted Ni [at%] can then be related to transformation temperature, M_s [K], by utilizing Eq. 19. Fig. 13 illustrates the comparison between predicted and experimental DSC-measured M_s.

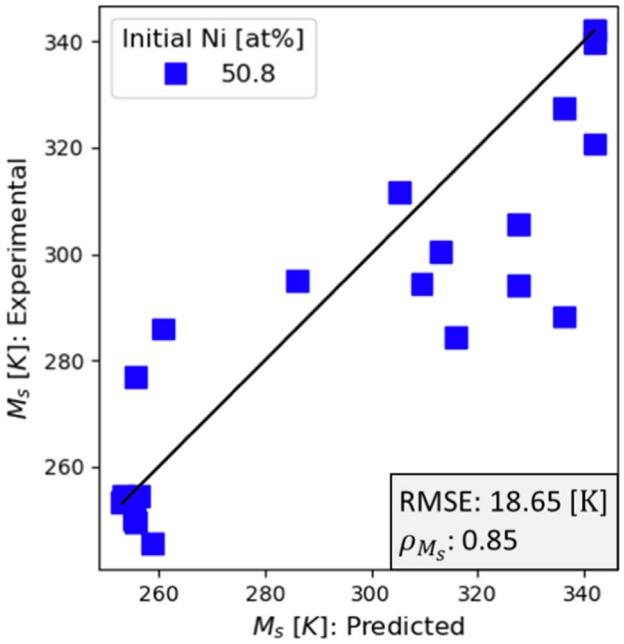

Fig. 13. Model predictions of M_s compared with empirical values for LPBF 50.8 Ni [at%] samples.

Table 5
Model parameters and thermophysical properties.

P (W)	υ (mm/s)	h (μm)	L_t (μm)	η	κ (W/m K)	C_p (J/kg K)	C	σ_x (μm)	ρ (kg/m^3)	T_0 (°C)	$f_{T_{melt}}$	$f_{T>T_{melt}}$
60–240	80–1330	70–130	40	0.61	28.9	1033.6	1.11	20	6471	23	3	30

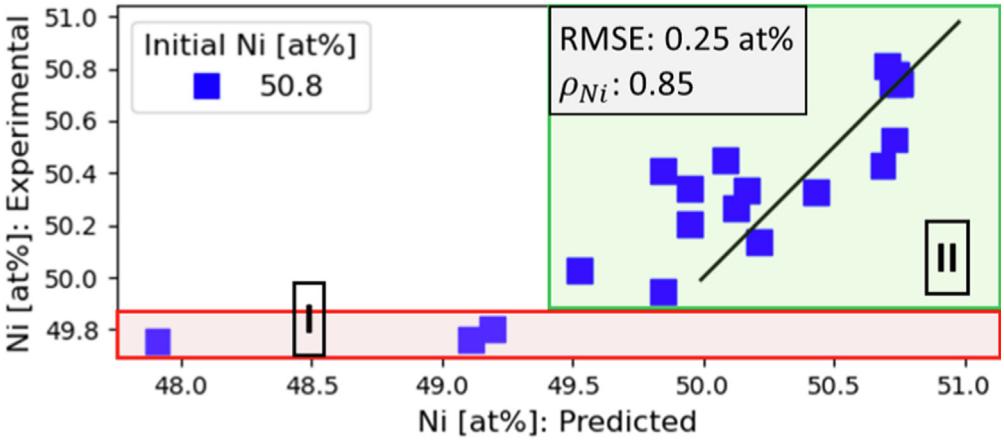

Fig. 12. Model predictions of Ni [at%] compared with experimental values for LPBF 50.8 Ni [at%] samples.

The RMSE for the 21 samples is 18.65 [K], which is again *well within* the range of uncertainty that a WDS or ICP-AES to M_s measurement might provide ($\pm$50 K). Additionally, the Pearson correlation, ρ_{M_s}, is 0.85, again suggesting a strong linear positive correlation between model predictions and experiment values. Due to the nature of the M_s-Ni relationship, errors in predicted Ni content are magnified with M_s, as is shown with several points predicting M_s values 30–45 K larger than corresponding empirical measurements. -However, some of this error could be imparted on the fact that the analytical M_s-Ni relationship is an approximation, and could be refined with supplementary experiments. Additionally, as mentioned earlier, the compounding effect of assumptions in the DSM-MLM-DEM could have impacted predicted values, some more-so than others. This requires further inspection of the relationship between processing parameters and structure, melt pool volume and surface area, as well as properties.

5. Conclusion

In metal AM, accurate resolution of the forward problem (predicting location-specific chemistry for a specific set of manufacturing processing parameters) is a necessary step preceding solution of the inverse problem (determining manufacturing processing conditions to achieve location-specific chemistry). With NiTi as a model material system, this first step is achieved by utilizing several hierarchically coupled physics-based models, calibration with experiments, and validation. The model chain begins with the DSM analytical model, enabling the simulation of thermal history based on processing parameters and material properties. A depth correction factor to account for the keyholing phenomenon, determined using an experimentally obtained criterion, is considered, and the DSM is calibrated against the width and depth measurements of $Ni_{51.2}Ti_{48.8}$ single-track experiments in the Bayesian context, providing a probabilistic calibrated value for heat capacity, conductivity, efficiency, and the depth correction coefficient. Following this, the DEM's initialization is 2-fold, where chemistry predictions are made for a melt pool based on the effect of evaporation and melt-pool overlap, and geometric considerations are evaluated and updated through the multi-layer model (MLM). By considering multiple-layers during the AM process, the effect of chemistry propagation due to melt pool overlap across a part is appropriately represented; followed by the combined consideration of the DSM-MLM-DEM that enables the prediction of Ni content in LPBF AM $Ni_{50.8}Ti_{49.2}$ parts with a smaller range of uncertainty (RSME: 0.25 Ni [at%]) than typical chemistry measurement techniques such as WDS and ICP-AES provide. Additionally, the martensitic transformation temperature, M_s, corresponding to these predictions were evaluated (RSME: 18.65 K), providing a complete transition from process to structure to properties. The DSM-MLM-DEM chain has thus shown its utility for predicting location-specific chemistry and solving the forward problem for LPBF AM $Ni_{50.8}Ti_{49.2}$, as well as providing a path to model NiTi's PSPP relationship.

Although the results here are promising, several considerations can be made for the improvement of this model and future work. The MLM is currently limited in its scope regarding the steady-state assumptions, where predictions could be improved by allowing for more complex patterns and full resolution of chemistry propagation. Additionally, the DSM's ability to switch processing parameters mid-scan would enable the modeling and chemistry prediction of more complex printing strategies and should be tested. From the computational perspective, the most important aspect in solving the inverse design problem is the introduction of a cheap and effective forward model. Full uncertainty propagation analysis through the coupled models is also needed to establish uncertainty bounds on predicted quantities. The current DSM-MLM-DEM will be tested in this regard to provide, potentially through training a cheaper surrogate model, processing parameters that will achieve a desired chemistry, and subsequently validated with experiments. In this context, the detection and quantification of prominent uncertainty sources in modeling are also essential tasks. Finally, as was mentioned in the Introduction, we will be using this forward model within an inverse design framework to achieve *designable and controllable* location-specific actuation in 3D-printed NiTi-based SMA components.

Data Availability

All data that support the findings of this study are openly available upon request.

Declaration of Competing Interest

The authors declare that they have no known competing financial interests or personal relationships that could have appeared to influence the work reported in this paper.

Acknowledgements

The authors would like to acknowledge the support of AFRL through the AFRL/TAMU Data-Enabled Discovery and Design of Materials (D^3EM) MLP program, under subcontract No. UTC-165852-19F5830-19-02-C1. Portions of this research were conducted with the advanced computing resources provided by Texas A&M High Performance Research Computing. PH acknowledges support from NSF through Grant No. 1849085. AE acknowledges support from NSF Grant No. 1846676. MR and RA acknowledge NSF through Grant No. 1545403.

References

[1] Nannan Guo, Ming C Leu, Additive manufacturing: technology, applications and research needs, Front. Mech. Eng. 8 (3) (2013) 215–243.
[2] Anton du Plessis, Chris Broeckhoven, Ina Yadroitsava, Igor Yadroitsev, Clive H. Hands, Ravi Kunju, Dhruv Bhate, Beautiful and functional: a review of biomimetic design in additive manufacturing, Addit. Manuf. 27 (2019) 408–427.
[3] John O Milewski, Additive manufacturing of metals. From Fundamental Technology to Rocket Nozzles, Medical Implants, and Custom Jewelry, 2017, pp. 134–157.
[4] H.L. Tarasankar DebRoy, JS Zuback Wei, T. Mukherjee, J.W. Elmer, J.O. Milewski, A. de Allison Michelle Beese, A De Wilson-Heid, W. Zhang, Additive manufacturing of metallic components–process, structure and properties, Prog. Mater Sci. 92 (2018) 112–224.
[5] X. He, Tarasankar DebRoy, P.W. Fuerschbach, Alloying element vaporization during laser spot welding of stainless steel, J. Phys. D: Appl. Phys. 36 (23) (2003) 3079.
[6] M.M. Collur, A. Paul, T. DebRoy, Mechanism of alloying element vaporization during laser welding, Metall. Trans. B 18 (4) (1987) 733–740.
[7] S.L. Semiatin, V.G. Ivanchenko, O.M. Ivasishin, Diffusion models for evaporation losses during electron-beam melting of alpha/beta-titanium alloys, Metall. Mater. Trans. B 35 (2) (2004) 235–245.
[8] Mohammad Ibraheem Khan, Andrew Pequegnat, Y. Norman Zhou, Multiple memory shape memory alloys, Adv. Eng. Mater. 15 (5) (2013) 386–393.
[9] J. Frenzel, Easo P. George, A. Dlouhy, Ch. Somsen, M.F.-X. Wagner, G. Eggeler, Influence of ni on martensitic phase transformations in niti shape memory alloys, Acta Mater. 58 (9) (2010) 3444–3458.
[10] Weijia Tang, Thermodynamic study of the low-temperature phase b19 and the martensitic transformation in near-equiatomic ti-ni shape memory alloys, Metall. Mater. Trans. A 28 (3) (1997) 537–544.
[11] Ji Ma, Brian Franco, Gustavo Tapia, Kubra Karayagiz, Luke Johnson, Jun Liu, Raymundo Arroyave, Ibrahim Karaman, Alaa Elwany, Spatial control of functional response in 4d-printed active metallic structures, Sci. Rep. 7 (2017) 46707.
[12] B.E. Franco, B. Ji Ma, GA Tapia Loveall, K. Karayagiz, J. Liu, A. Elwany, R. Arroyave, I. Karaman, A sensory material approach for reducing variability in additively manufactured metal parts, Sci. Rep. 7 (1) (2017) 1–12.
[13] J. Sam, B. Franco, J. Ma, I. Karaman, A. Elwany, J.H. Mabe, Tensile actuation response of additively manufactured nickel-titanium shape memory alloys, Scripta Mater. 146 (2018) 164–168.

[14] Ian D. McCue, Gianna M. Valentino, Douglas B. Trigg, Andrew M. Lennon, Chuck E. Hebert, Drew P. Seker, Salahudin M. Nimer, James P. Mastandrea, Morgana M. Trexler, Steven M. Storck, Realizing controlled, shape-morphing metallic components for deployable structures, Mater. Des. (2021) 109935.
[15] Kubra Karayagiz, Alaa Elwany, Gustavo Tapia, Brian Franco, Luke Johnson, Ji Ma, Ibrahim Karaman, Raymundo Arróyave, Numerical and experimental analysis of heat distribution in the laser powder bed fusion of ti-6al-4v, IISE Trans. 51 (2) (2019) 136–152.
[16] Patcharapit Promoppatum, P. Shi-Chune Yao, Chris Pistorius, Anthony D Rollett, Peter J Coutts, Frederick Lia, Richard Martukanitz, Numerical modeling and experimental validation of thermal history and microstructure for additive manufacturing of an inconel 718 product, Prog. Addit. Manuf. 3 (1) (2018) 15–32.
[17] Babis Schoinochoritis, Dimitrios Chantzis, Konstantinos Salonitis, Simulation of metallic powder bed additive manufacturing processes with the finite element method: A critical review, Proc. Inst. Mech. Eng. Part B: J. Eng. Manuf. 231 (1) (2017) 96–117.
[18] Gu. Dongdong, Beibei He, Finite element simulation and experimental investigation of residual stresses in selective laser melted ti–ni shape memory alloy, Comput. Mater. Sci. 117 (2016) 221–232.
[19] Y. Huang, L.J. Yang, X.Z. Du, Y.P. Yang, Finite element analysis of thermal behavior of metal powder during selective laser melting, Int. J. Therm. Sci. 104 (2016) 146–157.
[20] Sa.ad.A. Khairallah, Andrew T Anderson, Alexander Rubenchik, Wayne E King, Laser powder-bed fusion additive manufacturing: Physics of complex melt flow and formation mechanisms of pores, spatter, and denudation zones, Acta Mater. 108 (2016) 36–45.
[21] Loong-Ee Loh, Chee-Kai Chua, Wai-Yee Yeong, Jie Song, Mahta Mapar, Swee-Leong Sing, Zhong-Hong Liu, Dan-Qing Zhang, Numerical investigation and an effective modelling on the selective laser melting (slm) process with aluminium alloy 6061, Int. J. Heat Mass Transf. 80 (2015) 288–300.
[22] Yali Li, Gu. Dongdong, Parametric analysis of thermal behavior during selective laser melting additive manufacturing of aluminum alloy powder, Mater. Des. 63 (2014) 856–867.
[23] L. Dong, A. Makradi, S. Ahzi, Y. Remond, Three-dimensional transient finite element analysis of the selective laser sintering process, J. Mater. Process. Technol. 209 (2) (2009) 700–706.
[24] Serguei Kolossov, Eric Boillat, Rémy Glardon, P. Fischer, M. Locher, 3d fe simulation for temperature evolution in the selective laser sintering process, Int. J. Mach. Tools Manuf. 44 (2–3) (2004) 117–123.
[25] Panagis Foteinopoulos, Alexios Papacharalampopoulos, Panagiotis Stavropoulos, On thermal modeling of additive manufacturing processes, CIRP J. Manuf. Sci. Technol. 20 (2018) 66–83.
[26] Pengpeng Yuan, Gu. Dongdong, Molten pool behaviour and its physical mechanism during selective laser melting of tic/alsi10mg nanocomposites: simulation and experiments, J. Phys. D: Appl. Phys. 48 (3) (2015) 035303.
[27] Donghua Dai, Gu. Dongdong, Thermal behavior and densification mechanism during selective laser melting of copper matrix composites: Simulation and experiments, Mater. Des. 55 (2014) 482–491.
[28] Sankhya Mohanty, Jesper H Hattel, Numerical model based reliability estimation of selective laser melting process, Phys. Procedia 56 (2014) 379–389.
[29] Luke Johnson, Mohamad Mahmoudi, Bing Zhang, Raiyan Seede, Xueqin Huang, Janine T. Maier, Hans J. Maier, Ibrahim Karaman, Alaa Elwany, Raymundo Arróyave, Assessing printability maps in additive manufacturing of metal alloys, Acta Mater. 176 (2019) 199–210.
[30] Raiyan Seede, David Shoukr, Bing Zhang, Austin Whitt, Sean Gibbons, Philip Flater, Alaa Elwany, Raymundo Arroyave, Ibrahim Karaman, An ultra-high strength martensitic steel fabricated using selective laser melting additive manufacturing: Densification, microstructure, and mechanical properties, Acta Mater. 186 (2020) 199–214.
[31] John C Steuben, Andrew J Birnbaum, John G Michopoulos, Athanasios P Iliopoulos, Enriched analytical solutions for additive manufacturing modeling and simulation, Addit. Manuf. 25 (2019) 437–447.
[32] Jia-Ning Zhu, Evgenii Borisov, Xiaohui Liang, Eduard Farber, M.J.M. Hermans, V. A. Popovich, Predictive analytical modelling and experimental validation of processing maps in additive manufacturing of nitinol alloys, Addit. Manuf. 38 (2021) 101802.
[33] Edwin J Schwalbach, Sean P Donegan, Michael G Chapman, Kevin J Chaput, Michael A Groeber, A discrete source model of powder bed fusion additive manufacturing thermal history, Addit. Manuf. 25 (2019) 485–498.
[34] P. Honarmandi, R. Seede, L. Xue, D. Shoukr, P. Morcos, B. Zhang, C. Zhang, A. Elwany, I. Karaman, R. Arroyave, A rigorous test and improvement of the eagar-tsai model for melt pool characteristics in laser powder bed fusion additive manufacturing, Addit. Manuf. 47 (2021) 102300.
[35] John Goldak, Aditya Chakravarti, Malcolm Bibby, A new finite element model for welding heat sources, Metall. Trans. B 15 (2) (1984) 299–305.
[36] L. Xue, K.C. Atli, S. Picak, C. Zhang, B. Zhang, A. Elwany, R. Arroyave, I. Karaman, Controlling martensitic transformation characteristics in defect-free niti shape memory alloys fabricated using laser powder bed fusion and a process optimization framework, Acta Mater. (2021) 117017.
[37] Wayne E King, Holly D Barth, Victor M Castillo, Gilbert F Gallegos, John W Gibbs, Douglas E Hahn, Chandrika Kamath, Alexander M Rubenchik, Observation of keyhole-mode laser melting in laser powder-bed fusion additive manufacturing, J. Mater. Process. Technol. 214 (12) (2014) 2915–2925.
[38] Gennady G Gladush, Igor Smurov, Physics of laser materials processing: theory and experiment, vol. 146, Springer Science & Business Media, 2011.
[39] Heikki Haario, Eero Saksman, Johanna Tamminen, et al., An adaptive metropolis algorithm, Bernoulli 7 (2) (2001) 223–242.
[40] Pejman Honarmandi, Raymundo Arróyave, Uncertainty quantification and propagation in computational materials science and simulation-assisted materials design, Integr. Mater. Manuf. Innov. (2020) 1–41.
[41] Pejman Honarmandi, Noah H. Paulson, Raymundo Arróyave, Marius Stan, Uncertainty quantification and propagation in CALPHAD modeling, Model. Simul. Mater. Sci. Eng. 27 (3) (2019) 034003.
[42] Vahid Attari, Pejman Honarmandi, Thien Duong, Daniel J. Sauceda, Douglas Allaire, Raymundo Arroyave, Uncertainty propagation in a multiscale CALPHAD-reinforced elastochemical phase-field model, Acta Mater. 183 (2020) 452–470.
[43] P. Honarmandi, L. Johnson, R. Arroyave, Bayesian probabilistic prediction of precipitation behavior in Ni-Ti shape memory alloys, Comput. Mater. Sci. 172 (2020) 109334.
[44] Pejman Honarmandi, Thien Chi Duong, S. Fatheme Ghoreishi, Douglas Allaire, Raymundo Arroyave, Bayesian uncertainty quantification and information fusion in CALPHAD-based thermodynamic modeling, Acta Mater. 164 (2019) 636–647.
[45] P. Honarmandi, A. Solomou, R. Arroyave, D. Lagoudas, Uncertainty quantification of the parameters and predictions of a phenomenological constitutive model for thermally induced phase transformation in Ni–Ti shape memory alloys, Model. Simul. Mater. Sci. Eng. 27 (3) (2019) 034001.
[46] P. Honarmandi, R. Arroyave, Using bayesian framework to calibrate a physically based model describing strain-stress behavior of TRIP steels, Comput. Mater. Sci. 129 (2017) 66–81.
[47] Thien C. Duong, Robert E. Hackenberg, Alex Landa, Pejman Honarmandi, Anjana Talapatra, Heather M. Volz, Anna Llobet, Alice I. Smith, Graham King, Saurabh Bajaj, et al., Revisiting thermodynamics and kinetic diffusivities of uranium–niobium with bayesian uncertainty analysis, Calphad 55 (2016) 219–230.
[48] P.G. Klemens, R.K. Williams, Thermal conductivity of metals and alloys, Int. Met. Rev. 31 (1) (1986) 197–215.
[49] Brian Eelan Franco, Variability in the Shape Memory and Mechanical Response of Additively Manufactured NiTi. PhD thesis, 2019.
[50] Saul Dushman, Scientific foundations of vacuum technique, 1949.
[51] Carl L Yaws, The Yaws handbook of vapor pressure: Antoine coefficients, Gulf Professional Publishing, 2015.
[52] ASTM F2004-17, Standard test method for transformation temperature of nickel-titanium alloys by thermal analysis. Technical report, ASTM International, West Conshohocken, PA, 2017. https://doi.org/10.1520/F2004-17, https://www.astm.org.
[53] O. Benafan, G.S. Bigelow, D.A. Scheiman, Transformation behavior in niti-20hf shape memory alloys–transformation temperatures and hardness, Scripta Mater. 146 (2018) 251–254.
[54] Xinwei Wang, Karol Putyera, Accurate determination of the chemical composition of nickel-titanium binary alloys by nist high performance inductively coupled plasma – optical emission spectroscopy method, in: Shape Memory and Superelastic Technologies Conference (SMST), 2015.
[55] O. Benafan, G.S. Bigelow, A. Garg, R.D. Noebe, D.J. Gaydosh, R.B. Rogers, Processing and scalability of nitihf high-temperature shape memory alloys, Shape Memory Superelasticity (2021) 1–57.